Probing the flow- and magnetic-field-induced orientation of cellulose nanocrystals and magnetic nanoparticles via wide-angle X-ray scattering

Lina Sanchez-Botero[1], Alexey V. Dimov[2], Ruipeng Li[3], Detlef-M. Smilgies[3], and Juan P. Hinestroza[1,*]

[1] Fiber Science and Apparel Design, Cornell University, Ithaca, 14853, USA

[2] Meinig School of Biomedical Engineering, Cornell University, Ithaca, 14853, USA

[3] Cornell High Energy Synchrotron Source (CHESS), Cornell University, Ithaca, 14853, USA

*jh433@cornell.edu

ABSTRACT

We investigated the flow- and magnetic-field-induced orientation of cellulose nanocrystals (CNC) suspensions, pure and loaded with magnetite (Fe_3O_4) nanoparticles, using a custom-built flow cell that was placed in the D1 beamline of the Cornell High Energy Synchrotron Source. 2D wide-angle X-ray scattering (2D-WAXS) was used to quantify the direction and degree of orientation of the CNC suspensions under Poiseuille flow. We observed that the pure CNC suspensions and those with 1wt% Fe_3O_4 nanoparticles (NPs) exhibited very strong orientation along the flow direction. The CNC suspensions doped with higher concentrations of Fe_3O_4 NPs, 3wt%, showed different director-orientation patterns: isotropic, along the direction of flow, and bimodal. For these suspensions, the alignment along the flow direction occurs only at the highest values of apparent shear rates (60 s^{-1} and 100 s^{-1}) in the absence of magnetic field. Conversely, under the action of the magnetic field, the induced alignment along the flow occurs at low apparent shear rates, as low as 10 s^{-1}. We anticipate that these responsive effects to flow and magnetic fields may offer new approaches to tailor composite materials with magnetic anisotropic responses. It is hoped that further development of our exploratory work will translate these findings to the processing of composite materials with magnetic anisotropic responses.

INTRODUCTION

CNC are extensively used in the fabrication of high performance materials such as films[1,2], fibers[3], biomaterials[4], optical devices, as well as electronic devices and sensors[5–7]. Magnetic NPs have been used in medicine, catalysis, and biological studies[8–10]. Magnetic NPs have been found to enhance the thermal conductivity of heat exchange fluids[11], and their presence can enhance the magnetic response of diamagnetic polymers[12,13].

Recently, suspensions of NPs and liquid crystals (LC), such as those formed by CNC, have gained attention in the scientific literature due to their structural and optical properties, ability to self-assemble, and the possibility to control their structure through the application of external fields[13–17]. Composite suspensions of CNC and magnetite nanoparticles can exhibit properties not encountered in either one of the isolated components. For example, magnetic nanoparticles can be used to introduce changes in the magnetization of CNC suspensions, or, alternatively, the shape anisotropy of CNC can be used to manipulate the assembly of magnetite NPs[13,16,18–21]. However, practical realization of these possibilities would require a deeper understanding of the processing-structure-property relationships of the CNC-magnetite NP system. In this manuscript we report on the effect of flow rate, concentration, magnetic field and nanoparticle loading on the orientational structuring of suspensions of CNC and magnetite NPs.

EXPERIMENTAL SECTION

Materials: A slurry of cellulose nanocrystals (CNC) with a solids concentration of 11.8 wt% and 0.81 wt% of CNC surface-grafted sulfate, were purchased from the University of Maine and manufactured by the USDA Forest Service-Forest Products Laboratory, Madison, WI (FPL)[22]. Iron (III) chloride hexahydrate ($FeCl_3 \cdot 6H_2O$), Iron(II) chloride tetrahydrate ($FeCl_2 \cdot 4H_2O$) and Citric Acid were purchased from Sigma-Aldrich. ACS grade ammonium hydroxide (NH_4OH) was obtained from Macron Fine Chemicals (Center Valley, PA).

Synthesis of magnetite nanoparticles

Fe_3O_4 NPs were prepared via a co-precipitation method; 2.75 g of $FeCl_3 \cdot 6H_2O$ and 1.01 g of $FeCl_2 \cdot 4H_2O$ were dissolved in 100 mL of Milli-Q water and placed in a 500 mL three-necked flask.

2

The mixture was stirred at 100 rpm and heated to 80ºC. After heating, 3 mL of an ammonium hydroxide NH$_4$OH solution (25% w/w) were added dropwise and left to react for 20 min. Additional 75 mL of a NH$_4$OH solution (25% w/w) were added dropwise, and the total reaction time was approximately 100 min. The resulting black precipitate was decanted magnetically using a permanent magnet and was washed several times. The as-synthesized nanoparticles were immediately mixed with a citric acid aqueous solution (0.02 g/mL), and were under continuous stirring at 60°C for 90 min to obtain citric acid coated magnetite NPs. The resulting coated NPs were washed several times and dried in oven at 70°C.

Preparation of suspensions

The magnetite-CNC suspensions were prepared in two steps: first, magnetite NPs coated with citric acid were suspended (3 and 1 wt %) in water, and mixed with cellulose slurry solutions to obtain the desired CNC concentrations of 7 and 9 wt%. The pH of the CNC/NP suspensions was maintained in the range of 4-5. As a control system, magnetite-free CNC suspensions with concentrations of 7 wt% and 9 wt% were also used. All suspensions were prepared using Milli-Q water with a conductivity <18.2 MΩ·cm.

Custom-made Flow Cell

Figure 1a shows a schematic diagram of the device used in the experiments. The flow cell device was custom-built using an aluminum body with dimensions of 8.5 cm x 5 cm x 5 cm in length, width and height. At the side ends, the aluminum body was carefully machined so that it tapered to the diameter of strong neodymium iron boron ring magnets (K&J Magnetics RX828). The suspensions were studied using polyimide capillary tubing (Microlumen 390-111-5) with an internal diameter of 1 mm. A stainless-steel dispensing needle with a Luer Lock connection was attached to one side to the polyimide tubing (See supplemental Figure S1). The suspensions were driven into the capillary tube using a syringe pump (KD Scientific 410), programmed to the calculated flow rates.

We selected a Poiseuille flow system for which the flow rates (Q) are calculated using a chosen range of apparent shear rates as shown in Equation 1:

$$Q = \frac{\dot{\gamma}_{app}\pi r^3}{4} \tag{1}$$

The chosen apparent shear rates ($\dot{\gamma}_{app}$) ranged between 1 s^{-1} and 100 s^{-1} and the corresponding flow rates ranged between 5.7 and 343 µl/min (see supplemental Table S1). The quantity $\dot{\gamma}_{app}$, is the apparent shear rate of a non-Newtonian fluid (also referred to as wall shear rate in case of Newtonian fluids)[23].The Reynolds number is defined as the ratio of inertia forces to viscous forces (Equation 2):

$$Re = \frac{\rho \bar{v} D}{\mu} \tag{2}$$

where ρ is the fluid density, $\bar{v}$ is the average fluid velocity, D is the diameter of the channel, and μ is the fluid's dynamic viscosity.

For non-Newtonian fluids the suspension's viscosity changes as a function of shear rate following the Ostwald-de Waele power-law behavior as described in Equation 3:

$$\eta_{PL} = K\dot{\gamma}^{n-1} \tag{3}$$

where $\eta = \mu/\rho$ is the kinematic viscosity, K is the flow consistency index and n is the power-law (PL) flow behavior index.

A generalized Reynolds number[24] can be calculated for non-Newtonian fluids following the Ostwald-de Waele power-law behavior using equation 4:

$$Re_{genPL} = \frac{\rho D^n \bar{v}^{2-n}}{K((3n+1)/(4n))^n 8^{n-1}} \tag{4}$$

Calculated values for this generalized Reynolds number are reported in supplemental Table S1.

Another important part of the system's design was the calculation of the entrance length L_e. The entrance length determines the point after which the velocity profile becomes fully developed. This value can be calculated using equation 5[25].

$$\frac{L_e}{D} = \frac{0.6}{1+0.035 Re} + 0.056 Re \qquad (5)$$

Wide Angle X-ray Scattering (WAXS)

The custom-built flow cell was installed into the beamline D1 of the Cornell High Energy Synchrotron Source (CHESS) for two *in-situ* experiments. The experimental set-up is shown in Figures 1b and 1c. The measurements were performed in transmission geometry across the capillary (Figure 1a) using a monochromatic radiation of wavelengths of $\lambda = 1.155$ Å and $\lambda = 1.166$ Å (bandwidth $\Delta\lambda/\lambda$ of 1.5%) for the samples measured under static magnetic field and in the absence of it, respectively. The scattering patterns were collected by Hybrid Pixel Array Detector (HPAD) with a pixel size of 172 µm x 172 µm (Dectris Pilatus 200K). The distance between sample and detector was set to 189.12 mm for the experiments under static magnetic field and 165.36 mm for the experiments without magnetic field. The background flow data was obtained by filling the capillary tube with pure water. After recording the WAXS pattern of the water-filled tube, the water was removed and the capillary was dried with air. Before the experimental runs, each solution was pre-sheared at the lowest flow rate (5.7 µL/min) for 20 min without the application of magnetic field. After pre-shearing, the solution was pumped into the capillary tube at the flow rates corresponding to apparent shear rates of 1, 5, 10, 30 and 60 s^{-1}. This protocol was used to assure that all runs started with similar conditions. The azimuthal intensity profiles were extracted from the 2D-WAXS maps along ϕ for the reflection (200) of Cellulose I$_\beta$. This reflection peak is the most intense and does not overlap with air scattering halo of the direct beam around the beamstop or the detector's blind strip between its two active panels (horizontal black stripe in the 2D images). The Hermans Parameter[26] (S) is the order parameter in nematic fluids and characterizes the degree of orientation. S can be directly extracted from the diffraction data from the azimuth distribution function of the scattering intensity. This parameter is based on the second-order Legendre function of cosϕ, where ϕ is the azimuthal angle in a Debye-Scherrer ring and I(ϕ) is the angle dependent scattering intensity (Equations 6 and 7):

$$\langle cos^2\phi \rangle = \frac{\int_0^\pi I(\phi)cos^2\phi sin\phi d\phi}{\int_0^\pi I(\phi)sin\phi d\phi} \qquad (6)$$

$$S = \frac{3}{2}\langle cos^2\phi \rangle - \frac{1}{2} \qquad (7)$$

The parameter S varies between -1/2 and 1, where a value of S=0 corresponds to an isotropic orientation distribution, S=1 represents full alignment of all entities with respect to the director, and 0 < S <1 represents intermediate levels of anisotropic organization. Similarly, S= -1/2 indicates perfect antialignment, in which all entities lay within a plane orthogonal to the director. The 2D-WAXS spectra data were analyzed using Matlab.

Transmission Electron microscopy (TEM)

Transmission electron micrographs were obtained using a FEI Tecnai T12 system operating at 120kV. Specimens of CNC suspensions and magnetic nanoparticles were dropped on Lacey Film-Coated Grids supported by a carbon film. For negative staining of the CNC, a 2 wt% uranyl acetate solution was dropped on the grid, and the excess solution was removed using filter paper followed by air drying.

X-Ray Diffraction (XRD)

Dry samples of magnetite nanoparticles (Fe_3O_4) were characterized using a Scintag X-ray Diffractometer using Cu-Kα radiation (anode operating at 40 kV, 40 mA). The XRD patterns were recorded at room temperature with a step-size of 0.02º in the range of 10º–80º.

Magnetic Measurements

A physical properties measurement system (PPMS), equipped with a vibrating sample magnetometer (VSM), manufactured by Quantum Design, was used to collect zero-field-cooled (ZFC) and field-cooled (FC) magnetization curves from 5 K to 300 K in an applied field of 100 Oe.

Isothermal magnetizations and hysteresis loops were collected at temperatures of 300 K and 5 K for applied fields ranging from 20 kOe to -20 kOe. The dried samples were tightly packed in a VSM Powder Sample Holder (P125E).

Rheology measurements

The rheological behavior of the suspensions was investigated with TA instruments Discovery hybrid rheometer (DHR-3), using a cone and plate set-up (40 mm and 2º cone angle). Each solution was tested at shear rates from 0.1 to 300 s^{-1} at a constant temperature of 25ºC. All measurements were carried out in triplicate and using a solvent trap to avoid evaporation.

Thermogravimetric analysis (TGA)

TGA thermograms were recorded using a TA Instruments TGA 2950. The samples were heated from 30ºC to 900ºC at a rate of 10ºC/ min under a nitrogen atmosphere (40 mL/min) to minimize the mass increase of the specimen due to iron oxidation.

RESULTS AND DISCUSSION:

Magnetic nanoparticles.

The morphology of the synthesized Fe_3O_4 nanoparticles was investigated using transmission electron microscopy (TEM). Figure 2a corresponds to a TEM image of coated magnetite nanoparticles showing the presence of polydisperse spherical-shaped nanoparticles with an average diameter of 14±3 nm (See size distribution in supplemental Figure S2). The TEM image in Figure 2b corresponds to magnetite nanoparticles with CNC. Here we observed a rod-like morphology for CNC which typically show aggregation in TEM images after drying.[27] The length and width of the CNC were 127 ± 22 nm and 16.0 ± 3.5 nm which resulted in aspect ratios between 6.5 and 8.8 (see supplemental figure S2). Figure 2c shows the X-ray diffraction (XRD) patterns of the synthesized Fe_3O_4 nanoparticles coated with citric acid. All diffraction peaks can be indexed to the Fe_3O_4 phase (JCPDS, card no.: 00-019-0629). No other phases were detected in the pattern, reflecting the high purity of these Fe_3O_4 nanoparticles. The attachment of citric acid to the

surface of the magnetite nanoparticles was confirmed by TGA. The thermogram in Figure 2d indicates a two-step weight loss. The first stage occurs in the temperature range of 90-100°C due to water evaporation, and the second stage lays is in the 200−400 °C temperature range in which the decomposition of citric acid takes place[28]. For these experiments, we used nitrogen atmosphere to minimize iron oxidation hence allowing for a thermal decomposition of the citric acid.

The magnetization hysteresis loops of the Fe_3O_4 nanoparticles were obtained at temperatures of 5 K and 300 K, and at a maximum applied field of 20 kOe as shown in Figure 2e. The saturation magnetization values (M_S) for the Fe_3O_4 nanoparticles were 75.0 emu/g at 5 K and 62.0 emu/g at 300 K. These values are in good agreement with reports from literature for similar systems[29,30]. For example, Linh *et al.*[29] reported M_S values in the range 52-76 emu/g for Fe_3O_4 NPs with diameters of 14, 16, and 20 nm. Tahar *et al.*[30] reported M_S values of 69.51 emu/g at 300 K and 77.24 emu/g at 5 K for Fe_3O_4 NPs with a diameter of about 14 nm. The lower value of M_S for the NPs, when compared with the bulk measurements, could be a consequence of different contributions like surface disorder, spin canting and the large surface-to-volume ratio of small nanoparticles[31,32]. The superparamagnetic behavior of the synthesized Fe_3O_4 nanoparticles was confirmed by the almost negligible coercive field (Hc) at 300 K and the noticeable increase in the coercive field value (Hc) of the Fe_3O_4 nanoparticles at 5 K, which was approximately 221.3 Oe. This is a typical behavior expected for superparamagnetic systems[29,30,33]. Figure 1f shows the zero-field-cooling (ZFC) and the field-cooling (FC) measurements. The observed blocking temperature (T_B) was determined at 329 K, suggesting a blocking process for large particles. This blocking temperature can be associated with the formation of compact clusters and an increase of interactions between nanoparticles[29,30]. In this case, the nanoparticles are in close contact, and only the citric acid coating separates them. This blocking temperature is in agreement with values reported in the literature for similar systems[29,30,33].

Rheological properties

The rheological properties of the suspensions were characterized using a rheometer with a cone and plate geometry at 25ºC. We found that the viscosity of the suspensions depended strongly on the volume fraction of CNC and that of the magnetic nanoparticles. Figure 3a shows the viscosity as a function of shear rate for a 7 wt% CNC suspension and for a 7 wt% CNC suspension loaded with Fe_3O_4 nanoparticles at concentrations of 1 wt% and 3 wt%. The viscosity for the 7

8

wt% CNC suspension passes through the three regions which are associated with the polydomain texture of lyotropic liquid crystals[34]. In contrast, the 7 wt% CNC doped with Fe_3O_4 suspensions exhibit an increase in the magnitude of the viscosity values and clear shear thinning behavior. Figure 3b shows a plot of viscosity as a function of shear rate for the 9wt% CNC and a mixture of 9wt% CNC with Fe_3O_4 nanoparticles at concentrations 1 wt% and 3 wt%. All the suspensions display a shear-shinning behavior on the range of shear rates studied. For the 9 wt% CNC sample, this behavior can be attributed to gel formation at high concentrations of CNC, which hinders the formation of a chiral nematic phase[35]. However, the samples of 9 wt% CNC mixed with Fe_3O_4 NPs exhibit similar viscosity values for both loadings of 1 wt% and 3 wt% in the shear rate range of 100-300 s^{-1}. These observations demonstrate that the concentration of NPs plays major role in suspension dynamics. The NPs present in the more concentrated solutions tend to aggregate and cluster, increasing the number of interactions between particles, hence leading to an overall increase in viscosity. For rod-shape nanoparticles, such as those of the CNC, their arbitrary orientation results in a higher flow barrier and thus, an increase in the viscosity at low shear values[36,37].

Synchrotron Transmission WAXS Measurements

We investigated the flow induced orientation of the suspensions using a specially designed flow cell. The suspensions were subjected to a flow field and, in some cases, to both a flow field and a magnetic field parallel to the flow direction. 2D wide-angle X-ray scattering (2D-WAXS) was used to quantify direction and of the degree CNC orientation inside the capillary. For all specimens, the 2D-WAXS data showed at least 4 distinct scattering rings (Figure 4a). The radial integration of a 2D-WAXSpattern is shown in supplemental Figure S3, indicating the reflections (1-10), (110), (021) and (200) of monoclinic cellulose Iβ. The presence of the (021) reflection is consistent with literature[38,39] and can be ascribed to the transmission geometry. To probe the shear flow-induced arrangement of the CNC, the Herman's order parameter was calculated from the azimuthal variation of the scattering peak located at $q_{(200)} \approx 1.58$ Å^{-1} which corresponds to the equatorial (200) reflection of cellulose I_β.[2] The scattering vector associated with the (200) reflection is oriented perpendicular to the CNC long axis due to the monoclinic lattice; thus the reflection serves as a direct indicator of the orientation distribution function for the CNC and the nematic order parameter.[40] 2D-WAXS diffractograms obtained for the 7 wt% and 9 wt% CNC suspensions exhibit an anisotropic scattering pattern. A plot of the intensity along the (200) ring as a function of azimuthal angle ɸ (Figure 4b) shows that for both CNC concentrations the

9

intensity's maximum is centered at approximately $\phi \sim 90°$, suggesting that the predominant orientation of the CNCs is along the flow direction.

Figure 4c shows the behavior of the order parameter for a 7 wt% CNC suspension with and without magnetic field as a function of shear rate. It is clear that the CNC suspensions exhibit alignment along the flow (Fig 4 d-e) with a comparable degree of ordering regardless of the presence or absence of the magnetic field –the 7wt% CNC suspension reaches an alignment of S = 0.36 at a shear rate 60 s^{-1}. This degree of flow induced alignment is in agreement with those previously reported for CNC suspensions both experimentally[41,42] and theoretically[43]. We also found that in the absence of an external magnetic field, suspensions with higher concentrations of CNC, which are systems with stronger interparticle interactions, align more readily under shear when compared to the behavior of less concentrated suspensions. This is evident from the data presented in Figure 4f where the alignment for the 9wt% CNC suspension reaches an alignment of S = 0.48 at a shear rate of 60 s^{-1} and even at a low shear rate of 1s^{-1} some alignment can be observed[44,45]. In the absence of magnetic field, the order parameter for the 9wt% CNC suspension increases as a function of shear rate as illustrated in Figure 4h. However, when the same suspension flows under a magnetic field, the order parameter decreases as illustrated in Figure 4i. This behavior can be attributed to the competition between magnetic and viscous forces. It is well known that due to the negative diamagnetic anisotropy of the CNC, they tend to orient their long axis perpendicular to the direction of the magnetic field as illustrated in Figure 4g. Our scattering measurements confirm that under Poiseuille flow, the CNC align along the flow direction, as many systems of similar morphology do[46–49].

CNC suspensions loaded with 1wt% of magnetic nanoparticles

For the 7 wt% CNC suspension loaded with 1 wt% Fe_3O_4 NPs, the Herman's order parameter is lower than that of the 7 wt% CNC suspension without magnetic nanoparticles at all apparent shear rates. Furthermore, it was observed that this relation holds both in presence and absence of a magnetic field. Figure 5 suggest a negligible effect of the magnetic field over the orientation of the cellulose nanocrystals for this particular suspension. In contrast, the order parameter for the 9 wt% CNC suspension loaded with 1wt% Fe_3O_4 NPs measured under the presence of magnetic field decreases at shear rates between 1 and 10 s^{-1}, but it grows again at shear rates higher than 30 s^{-1} eventually reaching the same degree of orientation obtained during the flow experiments for the same suspension but without magnetic field. This unique behavior indicates

that the addition of only 1 wt% of Fe_3O_4 NPs has a significant impact on the orientation of the 9%wt CNC suspension, but when the same amount of NPs was added to the 7wt% CNC suspension the effect was almost negligible.

CNC suspensions loaded with 3wt% of magnetic nanoparticles

The shear response of the CNC suspensions become substantially more complex as we increase the concentration of magnetic nanoparticles in the suspensions. Figure 6 shows 2D-WAXS patterns of CNC suspensions loaded with 3 wt% Fe_3O_4 nanoparticles. Two notable changes in the WAXS patterns can be observed: first, the maximum of the (200) peak shifts from an azimuthal angle of 90° to 180° suggesting that a perpendicular orientation of the CNC is being induced (Figure 6b); secondly, the appearance of two intensity maxima – one at the meridian (ϕ=90°) and one at the equator (ϕ=180°) – suggesting the formation of a bimodally-oriented system (Figure 6c). To quantitatively analyze these changes, the relative azimuthal intensity distribution of the (200) reflections as a function of the apparent shear rate was plotted (Figure 7). Figure 7a shows the azimuthal intensity distributions for the 7 wt% CNC + 3 wt% Fe_3O_4 NPs suspension in the absence of magnetic field. In this case, the scattering intensity for the apparent shear rates between 1 – 30s^{-1} was mostly isotropic, with a broad scattering intensity maximum centered on the equator ($\phi \approx 180°$). At apparent shear rate of 60 s^{-1}, the system starts to align along the flow direction, which is indicated by the formation of the narrow intensity maximum on the meridian ($\phi \approx 90°$).

Figure 7b shows the azimuthal intensity distribution for the same 7 wt% CNC + 3 wt% Fe_3O_4 NPs suspension under a static magnetic field. For lower apparent shear rates (1 s^{-1} and 5 s^{-1}) the scattering intensity has one broad peak centered on the equator ($\phi \approx 180°$), but above 10 s^{-1} a significant amount of scattered intensity on the meridian ($\phi \approx 90°$) is observed. The width of the meridian peak progressively narrows with the increase of the shear rate suggesting that the CNC are being oriented along the flow direction. The order parameters corresponding to these measurements are reported in supplemental Table S1. Now, for the suspensions with higher concentration of CNC (9 wt% CNC) loaded with 3 wt% Fe_3O_4 NPs, a bimodal intensity distribution in the WAXS pattern can be observed as shown in Figures 7c and 7d. To characterize this system, a double Lorentz fitting of the curve and a peak area deconvolution analysis was performed in a similar manner to the method initially developed by Fujiyama *et al.*[50] *.* and improved later on by

Schrauwen et al.[51]. We used the area ratio [A*] between the meridional and equatorial peaks as an indicative of orientation of the CNC:

$$[A^*] = \frac{A^*}{A^* + C} \tag{8}$$

where C is the area of the peak around the azimuthal angle of 90^0 and A* is the area of the peak around 180^0. The angular spread of the orientation distribution function is correlated with the tilt variations of the CNC's long axes with regard to the flow direction. When the 9wt% CNC suspension loaded with 3wt% Fe_3O_4 NPs flows at lower shear rates ($1\ s^{-1}$), under the influence of a magnetic field, a mostly isotropic scattering pattern with a small orientation tendency to the equator ($\phi \approx 180\ °$) is observed, as shown in Figure 7d. At a shear rate of $5s^{-1}$, however, the sample exhibits a bimodal orientation. A further increase in the shear rate leads to narrowing of the intensity peak around the meridian ($\phi \approx 90^0$) achieving a maximum order parameter of S = 0.32. This degree of orientation is lower than the one achieved for the pure 9%wt CNC suspension, indicating that the presence of NPs distorts the alignment which is in agreement with previous observations in mixtures of liquid crystals and NPs[52–55]. As illustrated in Figure 7e and 7f and quantified in Table 1, in the absence of a magnetic field, the suspensions can exhibit either a unimodal (Figure 7e) or a bimodal orientation pattern (Figure 7f). When the suspension flows at higher rates, the CNC align along the flow direction as illustrated in Figure 7g and Figure 7h. It can be inferred that when small amounts of NPs are added to the CNC suspensions, the local arrangement of CNC is slightly distorted, but a further increase in the amount of NPs aggravates this distortion. We can also infer that when the CNC suspensions are loaded with magnetic nanoparticles and are under the influence of both magnetic and flow fields, there are three competing orientational mechanisms: 1. The flow field tends to align the CNC long axis in a direction parallel to the flow, 2. the magnetic moment of the magnetic nanoparticles will align along the external field (dipole mechanism) and 3. The CNC director tends to align perpendicular to the applied magnetic field due to the negative diamagnetic anisotropy of the nanocrystals. Although the distortion induced by moderate magnetic fields on CNC is usually very weak, it has been reported that at high concentrations of CNC and within a constrained geometry, the CNC do orient perpendicular to the magnetic field[45]. This orientational mechanism can explain the behavior of the 9wt% CNC suspension. Another effect of the presence of the magnetic field is the induced dipolar interaction of the magnetic nanoparticles. When the dipolar interaction energy

12

between the nanoparticles exceeds their thermal energy, the particles will form linear chain-like aggregates aligned along the direction of the magnetic field. In our experiments, we noted that the dipolar interaction and the chain-formation effect is strong. Namely, in the presence of an external magnetic field the flow rate required to induce alignment along the flow direction is lower than the one required for the case without the influence of magnetic field. Our experimental results also show that the nanoparticles can affect the orientational order of a macroscopic medium, in this case, the CNC suspension.

CONCLUSIONS

In this work, the structure-orientation of CNC suspensions doped with magnetite (Fe_3O_4) nanoparticles was studied experimentally using synchrotron wide-angle x-ray scattering. The experimental data indicate that the assembly of CNC can be efficiently manipulated by the shear rate, magnetic field and nanoparticle doping. Our results also show that pure CNC (7wt% and 9wt%) suspensions adopt a nematic phase induced by the flow field and exhibit relatively high values of the Herman's order parameter due to the anisotropic shape ad high aspect ratio of the CNC. The particle system resulting from the CNC-Fe_3O_4 NPs mixing is sensitive to the concentrations of the components. For example, suspensions with lower concentrations of Fe_3O_4 NPs (1wt%) more readily display flow-induced CNC orientation and appear to be less sensitive to the presence of a magnetic field. As a result, the flow induces anisotropic orientation along its direction at low shear rates. An increase in Fe_3O_4 NPs (3wt%) results in more intricate particle dynamics which leads to the formation of isotropic or bimodal orientations. However, isotropic or bimodal alignments are broken down at higher shear rates. We hypothesize the existence of three competing orientation mechanisms: 1. The flow field tends to align the CNC's long axis parallel to the flow, 2. the magnetic moments of the magnetic nanoparticles align along the external field (dipole mechanism) and 3. the director tends to align perpendicular to the applied magnetic field due to the negative diamagnetic anisotropy of the CNC. The latter mechanism is strongly dependent on the CNC concentration in the suspension and was observed only for experiments with the higher concentration of CNC (9wt%) in pure suspensions. At low concentrations of Fe_3O_4 NPs (1wt%) only the first orientation mechanism is dominant, while at high Fe_3O_4 NPs (3wt%) concentration the effects of the first and second mechanisms were manifested. These responsive effects of flow and magnetic fields may offer new approaches to manufacture composite materials with unique magnetic anisotropic responses.

Table 1. Hermans order parameter for CNC suspensions doped with 3 wt% magnetite (Fe_3O_4) during flow-induced assembly at different apparent shear rates.

| Sample	Magnetic Field	Apparent shear rate	Order parameter at 90º	Order parameter at 180º	Area ratio
7 wt% CNC + 3wt% Fe_3O_4	0	1	-	-0.068 ± 0.003	-
		5	-	-0.060 ± 0.005	-
		10	-	-0.047 ± 0.009	-
		30	-	-0.040 ± 0.022	-
		60	0.189 ± 0.038	-	-
	0.45 T	1	-	-0.055 ± 0.012	-
		5	-	-0.013 ± 0.003	-
		10	0.230 ± 0.013	-	-
		30	0.254 ± 0.013	-	-
		60	0.312 ± 0.031	-	-
9 wt% CNC + 3wt% Fe_3O_4	0	1	0.154 ± 0.027	-0.179 ± 0.006	0.298
		5	0.133 ± 0.052	-0.135 ± 0.016	0.917
		10	0.093 ± 0.005	-0.177 ± 0.007	0.80477
		30	0.217 ± 0.034	-0.137 ± 0.008	0.63087
		60	0.204 ± 0.022	-0.124 ± 0.011	0.47113
		100	0.372 ± 0.012	-	-
	0.45 T	1		-0.068 ± 0.004	
		5	0.275 ± 0.025	-0.349 ± 0.002	0.16933
		10	0.315 ± 0.012	-	-
		30	0.270 ± 0.021	-	-
		60	0.317 ± 0.009	-	-

FIGURES
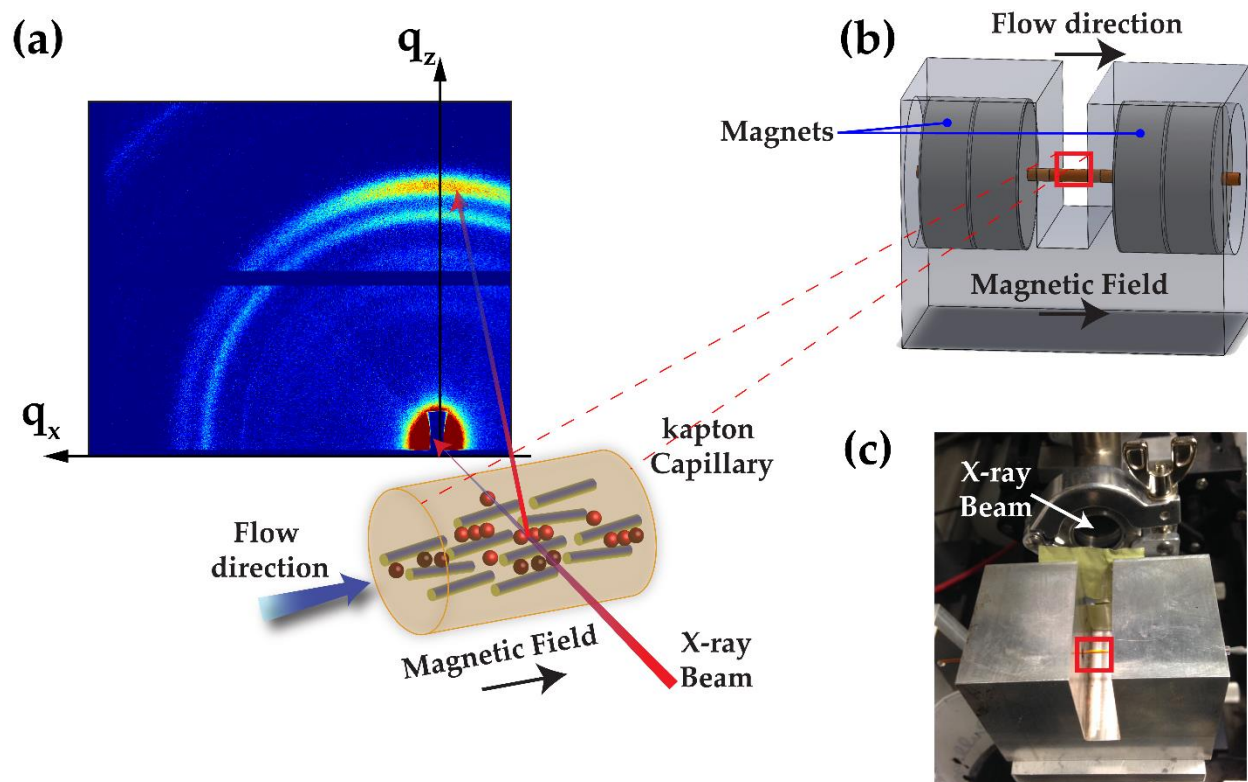
Figure 1: (a) Schematic diagram of small volume flow cell device composed of polyimide capillary, magnets and aluminum body. (b) Schematic diagram of experimental set-up and (c) real picture of the system setup for in situ transmission Wide-Angle X-ray Scattering (WAXS) experiment at CHESS beamline D1. Scattering patterns were recorded at each apparent shear rate in the center of the polyimide capillary.
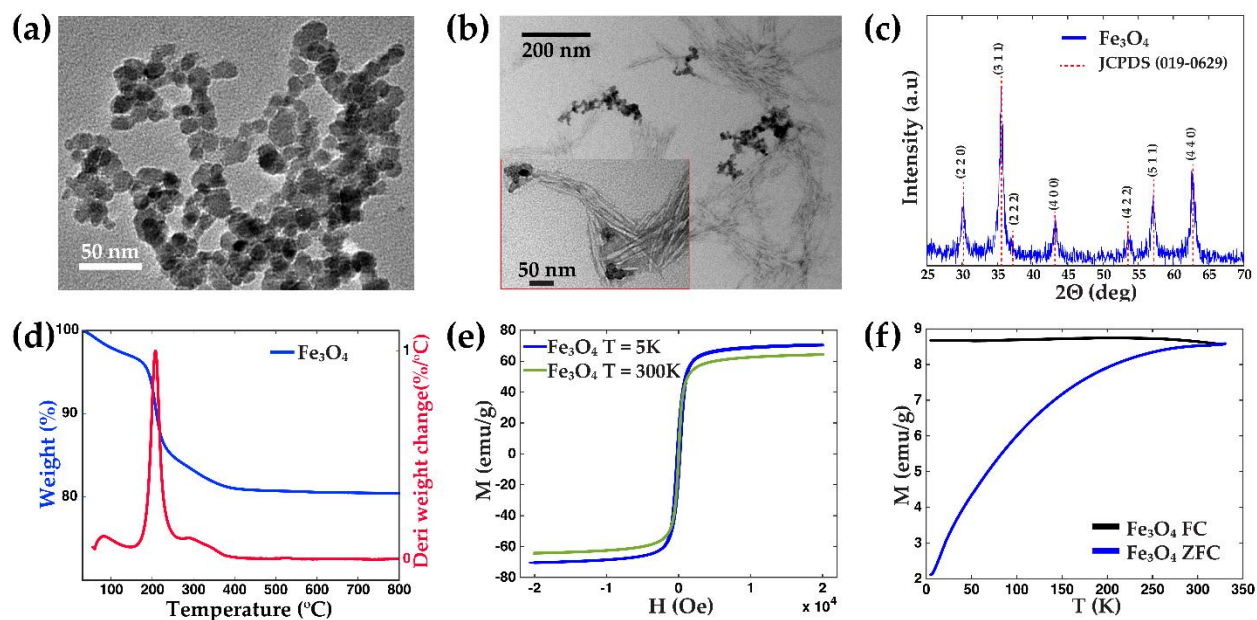
Figure 2: Characterization of magnetite (Fe$_3$O$_4$) NPs and CNC (a) Transmission Electron micrograph of magnetite Fe$_3$O$_4$ NPs. (b) Transmission Electron micrographs of a mixture of CNC stained with uranyl acetate and Fe$_3$O$_4$ NPs. (c) X-ray Diffraction pattern of magnetite NPs. (d) Thermogravimetric analysis of the Fe$_3$O$_4$ NPs (e) Magnetization vs Field for Fe$_3$O$_4$ NPs recorded at 5 and 300 K (f) Zero field cooled (index ZFC) and field-cooled (FC) magnetization of Fe$_3$O$_4$ particles in an applied field of 100 Oe.
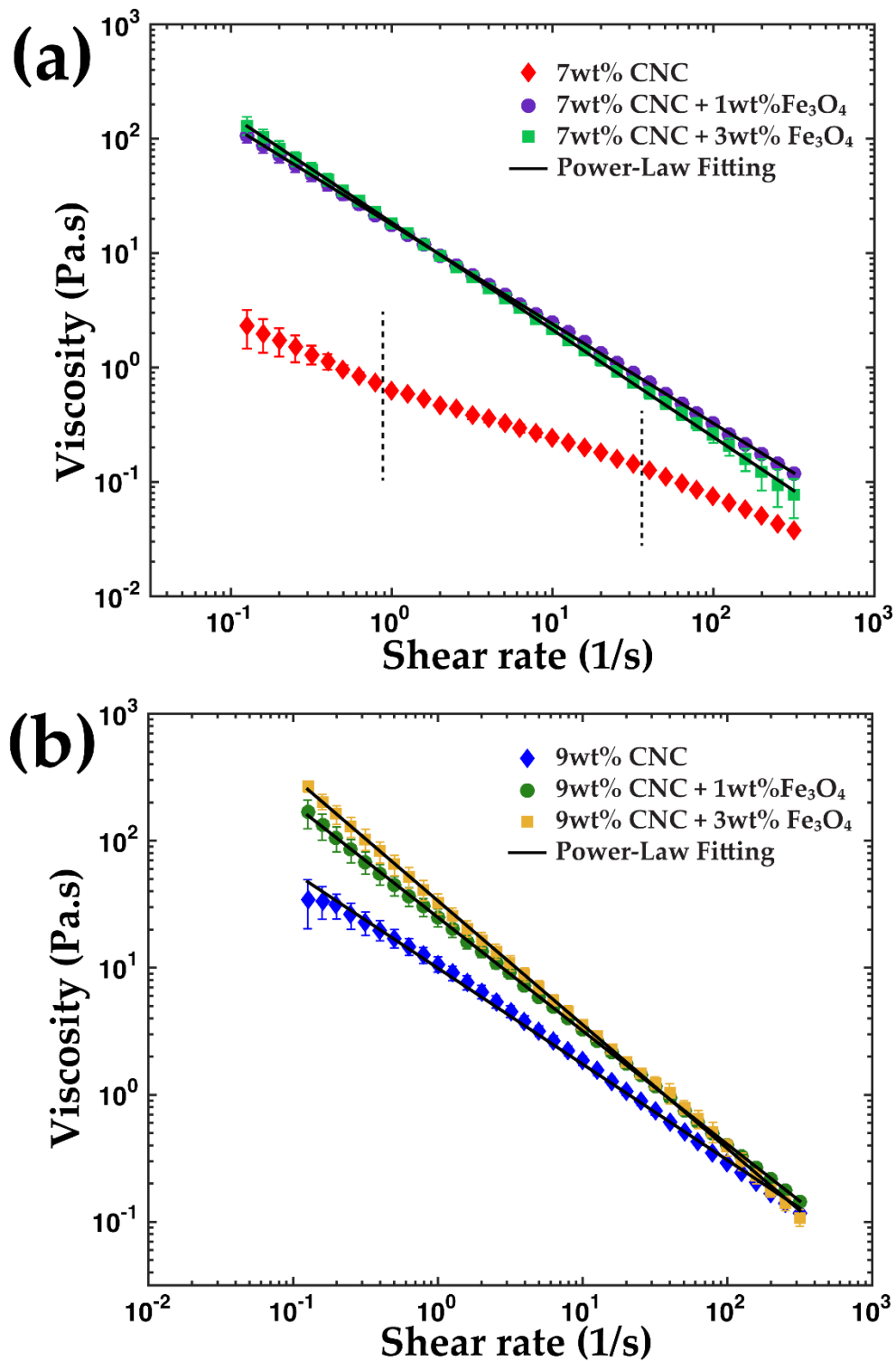
Figure 3: Viscosity vs shear rate for pure CNC and composite CNC-Fe$_3$O$_4$ suspensions. CNC concentrations were (a) 7 wt% CNC and (b) 9 wt% CNC.
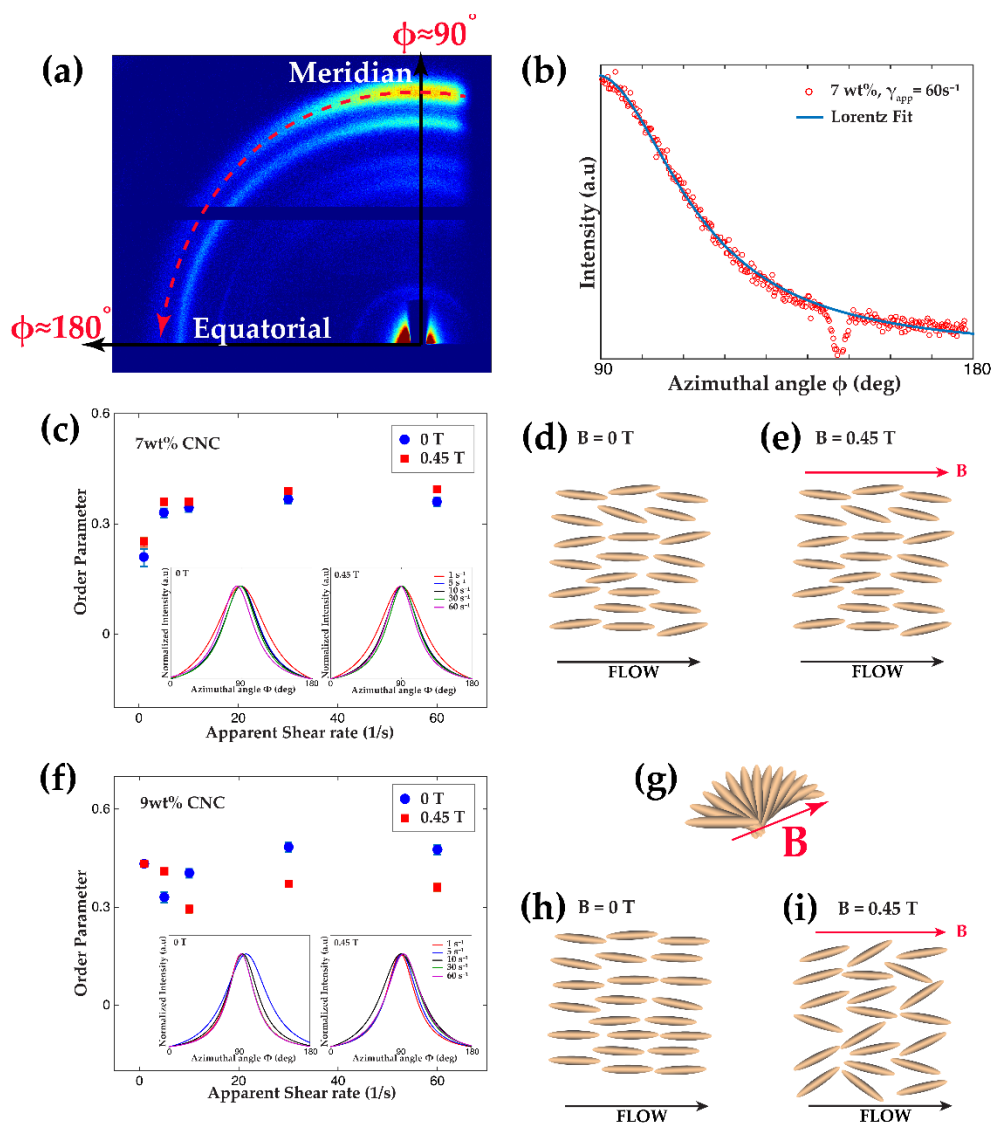
Figure 4: (a) 2D WAXS intensity map for the 7 wt% CNC at an apparent shear rate of 60 s^{-1}, (b) Azimuthal intensity profile of (200) (across black dashed line in a) and the best-fit Lorentzian curve used to calculate the order parameters. (c) Order parameters as a function of apparent shear rates, with and without magnetic field of 7 wt% CNC (d) schematic illustration of 7wt% CNC suspension alignment along the flow at B=0 T (e) and B=0.45 T (f) Order parameters as a function of apparent shear rates, with and without magnetic field of 9wt% CNC (g) schematic model of the chiral nematic phase orientation of CNC under the application of a magnetic field, i.e.

18

representation of the CNC diamagnetic response (h) schematic illustration of 9wt% CNC suspension alignment along the flow at B=0 T and (i) at B=0.45 T. The insets correspond to the azimuthal intensity profiles across the main peak (200).
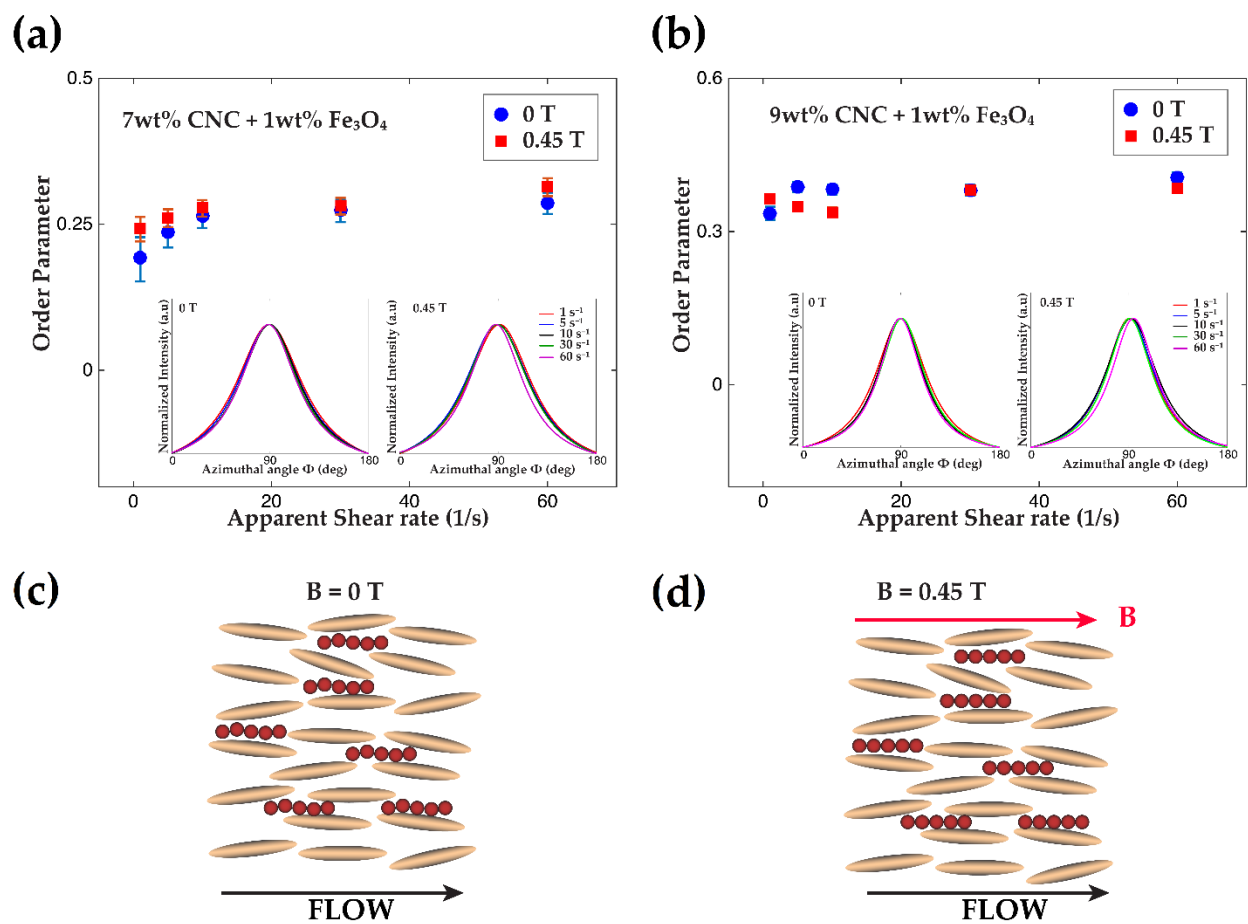

Figure 5. Order parameters as a function of apparent shear rates, with and without magnetic field of (a) 7wt% CNC +1wt% Fe_3O_4 and (b) 9 wt% CNC +1wt% Fe_3O_4. The insets correspond to the azimuthal intensity profiles across the main peak (200). The model for the alignment without magnetic field and under magnetic field are shown in panels (c) and (d), respectively.
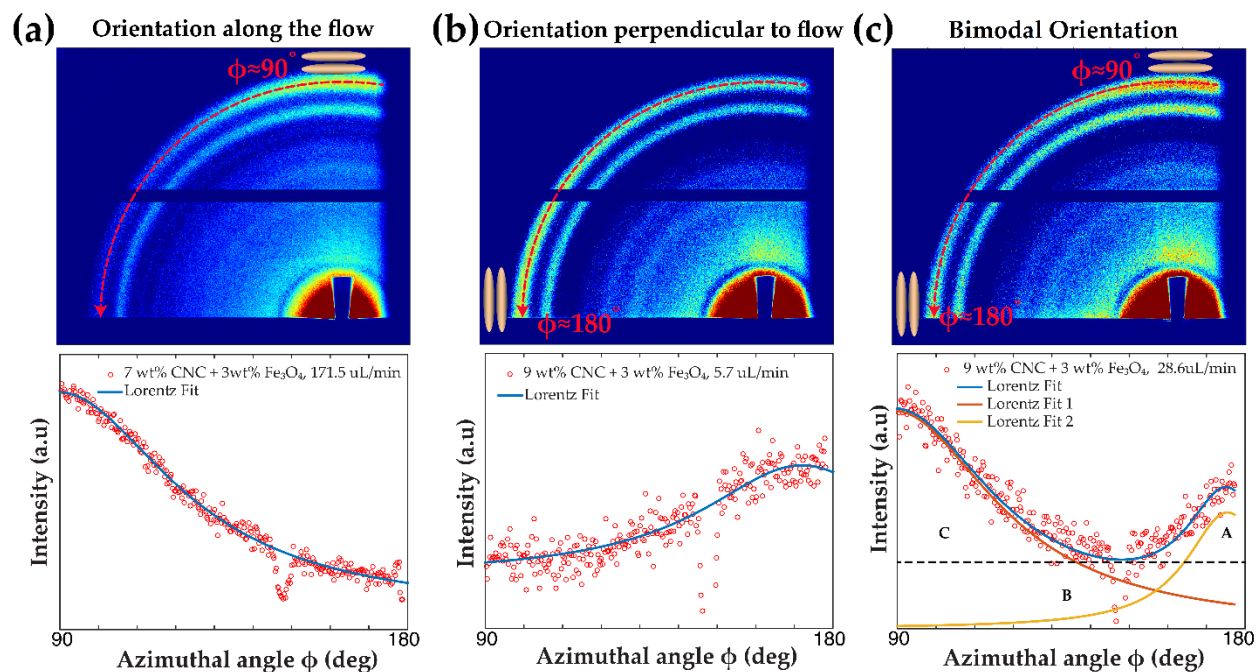
Figure 6. Schematic diagram showing the relationship between CNC orientation and the resulting 2D-WAXS patterns: (a) CNC oriented mostly parallel to the flow direction; (b) CNC oriented mostly perpendicular to the flow direction; (c) bimodal orientation of CNC. The lower panel shows the corresponding azimuthal profiles at q = 1.58 Å^{-1} or to the (200) peak of CNC. The corresponding fit is plotted as a solid line on top of the data. (See supplemental Figure S4 for radial profiles with reflections (1-10), (110), (021), and (200) of monoclinic cellulose Iβ indicated.)
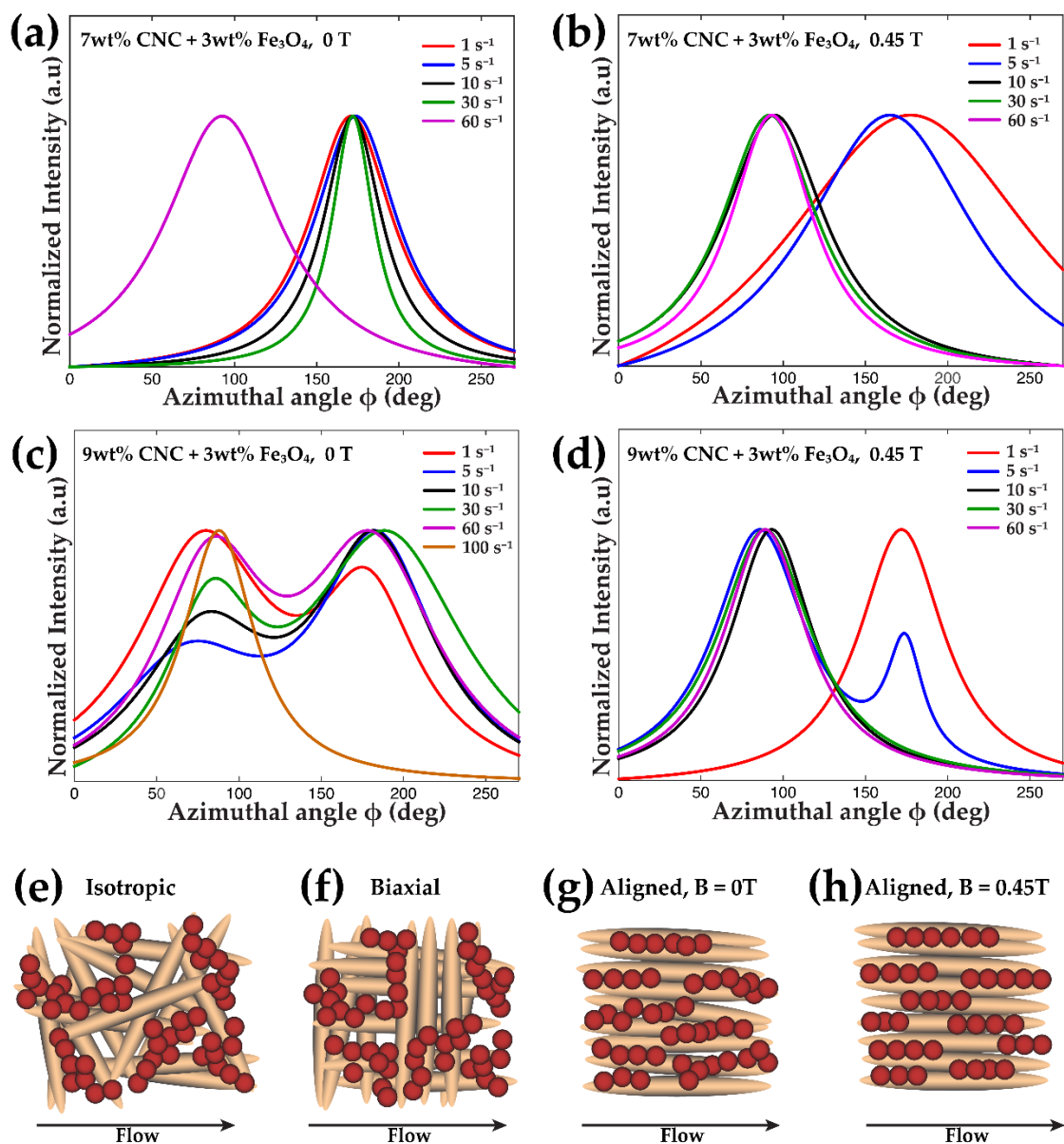
20

Figure 7. Normalized azimuthal intensity curves (200) reflections as a function of apparent shear rate for (a) 7 wt% CNC, + 3wt% Fe_3O_4, B=0T, (b) 7 wt% CNC, + 3wt% Fe_3O_4, B=0.45T, (d) 9 wt% CNC, + 3wt% Fe_3O_4, B=0T, (e) 9 wt% CNC, + 3wt% Fe_3O_4, B = 0.45T. A schematic illustration of the orientation of CNC suspensions doped with a 3wt% Magnetite: (e) isotropic orientation (f) bimodal orientation (g) aligned along the flow without magnetic field (0 T) and (d) aligned along the flow under magnetic field (0.45T). The black arrows represent the direction of the flow. The orientation of the CNC-Fe_3O_4 system is exaggerated to illustrate the orientation effects in each case.

REFERENCES

1. Diaz, J. a, Wu, X., Martini, A., Youngblood, J. P. & Moon, R. J. Thermal Expansion of Self-Organized and Shear-Oriented Cellulose Nanocrystal Films. *Biomacromolecules* **14**, 2900–2908 (2013).

2. Sanchez-Botero, L., Dimov, A. V., Li, R., Smilgies, D. M. & Hinestroza, J. P. In Situ and Real-Time Studies, via Synchrotron X-ray Scattering, of the Orientational Order of Cellulose Nanocrystals during Solution Shearing. *Langmuir* **34**, 5263–5272 (2018).

3. Håkansson, K. M. O. *et al.* Hydrodynamic alignment and assembly of nanofibrils resulting in strong cellulose filaments. *Nat. Commun.* **5**, (2014).

4. Wondraczek, H. & Heinze, T. Cellulosic Biomaterials. in *Polysaccharides* 1–34 (2014). doi:10.1007/978-3-319-03751-6

5. Barras, R. *et al.* Printable cellulose-based electroconductive composites for sensing elements in paper electronics. *Flex. Print. Electron.* **2**, (2017).

6. Golmohammadi, H., Morales-Narváez, E., Naghdi, T. & Merkoçi, A. Nanocellulose in Sensing and Biosensing. *Chem. Mater.* **29**, 5426–5446 (2017).

7. Kim, J.-H., Mun, S., Ko, H.-U., Yun, G.-Y. & Kim, J. Disposable chemical sensors and biosensors made on cellulose paper. *Nanotechnology* **25**, 092001 (2014).

8. Bellizzi, G. & Bucci, O. M. Magnetic Nanoparticle Hyperthermia. in *Emerging Electromagnetic Technologies for Brain Diseases Diagnostics, Monitoring and Therapy* (eds. Crocco, L., Karanasiou, I., James, M. L. & Conceição, R. C.) 129–191 (Springer International Publishing, 2018). doi:10.1007/978-3-319-75007-1_6

9. Cantillon-Murphy, P., Wald, L. L., Adalsteinsson, E. & Zahn, M. Simulating Magnetic Nanoparticle Behavior in Low-field MRI under Transverse Rotating Fields and Imposed Fluid Flow. *J. Magn. Magn. Mater.* **322**, 2607–2617 (2010).

10. Voltairas, P. a, Fotiadis, D. I. & Michalis, L. K. Hydrodynamics of magnetic drug targeting. *J. Biomech.* **35**, 813–21 (2002).

11. Gan Jia Gui, N., Stanley, C., Nguyen, N. T. & Rosengarten, G. Ferrofluids for heat transfer enhancement under an external magnetic field. *Int. J. Heat Mass Transf.* **123**,

110–121 (2018).

12. Sklute, E. C. *et al.* Orientation of diamagnetic layered transition metal oxide particles in 1-tesla magnetic fields. *J. Am. Chem. Soc.* **133**, 1824–31 (2011).

13. Vallooran, J. J., Bolisetty, S. & Mezzenga, R. Macroscopic alignment of lyotropic liquid crystals using magnetic nanoparticles. *Adv. Mater.* **23**, 3932–7 (2011).

14. Brochard, F. & de Gennes, P. G. Theory of Magnetic Suspensions in Liquid Crystals. *J. Phys.* **31**, 691–708 (1970).

15. Mertelj, A. & Lisjak, D. Ferromagnetic nematic liquid crystals. *Liq. Cryst. Rev.* **5**, 1–33 (2017).

16. Gdovinová, V. *et al.* Influence of the anisometry of magnetic particles on the isotropic–nematic phase transition. *Liq. Cryst.* **41**, 1773–1777 (2014).

17. Prodanov, M. F. *et al.* Dispersion of magnetic nanoparticles in a polymorphic liquid crystal. *Liq. Cryst.* **39**, 1512–1526 (2012).

18. Yoshitake, H., Sugimura, K., Teramoto, Y. & Nishio, Y. Magnetic property of oriented films of cellulose nanocrystal/carrageenan composites containing iron oxide nanoparticles: Effect of anisotropic aggregation of the nanoparticles. *Polymer (Guildf).* **99**, 147–156 (2016).

19. Tomašovicová, N. *et al.* Alternating current magnetic susceptibility of a ferronematic. *Beilstein J. Nanotechnol.* **8**, 2515–2520 (2017).

20. Wang, M., He, L., Zorba, S. & Yin, Y. Magnetically actuated liquid crystals. *Nano Lett.* **14**, 3966–3971 (2014).

21. Sakai, R., Teramoto, Y. & Nishio, Y. Producing a magnetically anisotropic soft material: Synthesis of iron oxide nanoparticles in a carrageenan/PVA matrix and stretching of the hybrid gelatinous bulk. *Polym. J.* **50**, 251–260 (2018).

22. Reiner, R. S. & Rudie, A. W. Process Scale-Up of Cellulose Nanocrystal Production to 25 kg per Batch at the Forest Products Laboratory. *Prod. Appl. Cellul. Nanomater.* 21–24 (2013).

23. Morrison, F. A. *Understanding Rheology.* (Oxford University Press Inc., New York, 2001).

24. Madlener, K., Frey, B. & Ciezki, H. K. Generalized reynolds number for non-newtonian

fluids. *Prog. Propuls. Phys.* **1**, 237–250 (2009).

25. Janna, W. S. *Introduction to Fluid Mechanics, Fourth Edition*. (CRC Press, Taylor & Francis group, 2010).

26. J. J. Hermans P. H. Hermans D. Vermaas A. Weidinger. Quantitative Evaluation of Orientation in Cellulose Fibres From The X-Ray Fibre Diagram. *Recl. des Trav. Chim. des Pays-Bas banner* **65**, 427–447 (1946).

27. Habibi, Y., Lucia, L. a & Rojas, O. J. Cellulose nanocrystals: chemistry, self-assembly, and applications. *Chem. Rev.* **110**, 3479–500 (2010).

28. Sahoo, Y. *et al.* Aqueous ferrofluid of magnetite nanoparticles: Fluorescence labeling and magnetophoretic control. *J. Phys. Chem. B* **109**, 3879–85 (2005).

29. Linh, P. H., Manh, D. H., Phong, P. T., Hong, L. V. & N.X., P. Magnetic Properties of Fe3O4 Nanoparticles Synthesized by Coprecipitation Method. *J. Supercond. Nov. Magn.* **27**, 2111–2115 (2014).

30. Tahar, L. Ben, Oueslati, M. H. & Abualreish, M. J. A. Synthesis of magnetite derivatives nanoparticles and their application for the removal of chromium (VI) from aqueous solutions. *J. Colloid Interface Sci.* **512**, 115–126 (2018).

31. Krycka, K. L. *et al.* Origin of Surface Canting within Fe3O4 Nanoparticles. *Phys. Rev. Lett.* **113**, 147203 (2014).

32. *Complex Magnetic Nanostructures*. (Springer International Publishing, 2017). doi:10.1007/978-3-319-52087-2

33. Xu, Y. Y. *et al.* A simplified method for synthesis of Fe3O4@PAA nanoparticles and its application for the removal of basic dyes. *Appl. Surf. Sci.* **258**, 3897–3902 (2012).

34. Onogi, S. & Asada, T. *Rheology and Rheo-Optics of Polymer Liquid Crystals. In Proceedings of the Eighth International Congress on Rheology* (Plenum Press, 1980). doi:10.1007/978-1-4684-3740-9_9

35. Gray, D. Recent Advances in Chiral Nematic Structure and Iridescent Color of Cellulose Nanocrystal Films. *Nanomaterials* **6**, 213 (2016).

36. Wierenga, A. M. & Philipse, A. P. Low-shear viscosity of isotropic dispersions of (Brownian) rods and fibres; a review of theory and experiments. *Colloids Surfaces A*

Physicochem. Eng. Asp. **137**, 355–372 (1998).

37. Cassagnau, P. Linear viscoelasticity and dynamics of suspensions and molten polymers filled with nanoparticles of different aspect ratios. *Polymer (Guildf).* **54**, 4762–4775 (2013).

38. French, A. D. & Santiago Cintrón, M. Cellulose polymorphy, crystallite size, and the Segal Crystallinity Index. *Cellulose* **20**, 583–588 (2013).

39. Segal, L., Creely, J. J., Martin, A. E. & Conrad, C. M. An Empirical Method for Estimating the Degree of Crystallinity of Native Cellulose Using the X-Ray Diffractometer. *Text. Res. J.* **29**, 786–794 (1959).

40. Guenoun, G., Schmitt, N., Roux, S., Régnier, G. Crystalline orientation assessment in transversely isotropic semicrystalline polymer: Application to oedometric compaction of PTFE. P*olymer Engineering and Science*, 2021, **61**, 107-114 (2021).

41. Brouzet, C., Mittal, N., Söderberg, L. D. & Lundell, F. Size-Dependent Orientational Dynamics of Brownian Nanorods. *ACS Macro Lett.* **7**, 1022–1027 (2018).

42. Shafiei-Sabet, S., Hamad, W. Y. & Hatzikiriakos, S. G. Rheology of nanocrystalline cellulose aqueous suspensions. *Langmuir* **28**, 17124–33 (2012).

43. Noroozi, N., Grecov, D. & Shafiei-Sabet, S. Estimation of viscosity coefficients and rheological functions of nanocrystalline cellulose aqueous suspensions. *Liq. Cryst.* **41**, 56–66 (2014).

44. Orts, W. J., Godbout, L., Marchessault, R. H. & Revol, J. F. Enhanced Ordering of Liquid Crystalline Suspensions of Cellulose Microfibrils : A Small Angle Neutron Scattering Study. *Macromolecules* **31**, 5717–5725 (1998).

45. De France, K. J., Yager, K. G., Hoare, T. & Cranston, E. D. Cooperative Ordering and Kinetics of Cellulose Nanocrystal Alignment in a Magnetic Field. *Langmuir* **32**, 7564–7571 (2016).

46. Cha, Y. J., Kim, D. S. & Yoon, D. K. Highly Aligned Plasmonic Gold Nanorods in a DNA Matrix. *Adv. Funct. Mater.* **27**, 1–8 (2017).

47. Xie, D., Lista, M., Qiao, G. G. & Dunstan, D. E. Shear Induced Alignment of Low Aspect Ratio Gold Nanorods in Newtonian Fluids. *J. Phys. Chem. Lett.* **6**, 3815–3820 (2015).

48. Thorkelsson, K., Bai, P. & Xu, T. Self-assembly and applications of anisotropic nanomaterials: A review. *Nano Today* **10**, 48–66 (2015).

49. Kuncicky, D. M., Naik, R. R. & Velev, O. D. Rapid deposition and long-range alignment of nanocoatings and arrays of electrically conductive wires from tobacco mosaic virus. *Small* **2**, 1462–1466 (2006).

50. Fujiyama, M., Wakino, T. & Kawasaki, Y. Structure of skin layer in injection-molded polypropylene. *J. Appl. Polym. Sci.* **35**, 29–49 (1988).

51. Schrauwen, B. A. G. *et al.* Structure, Deformation, and Failure of Flow-Oriented Semicrystalline Polymers. *Macromolecules* **37**, 8618–8633 (2004).

52. Wood, T. A., Lintuvuori, J. S., Schofield, A. B., Marenduzzo, D. & Poon, W. C. K. A Self-Quenched Defect Glass in a Colloid-Nematic Liquid Crystal Composite. *Science (80-.).* **334**, 79–83 (2011).

53. Whitmer, J. K., Joshi, A. A., Roberts, T. F. & de Pablo, J. J. Liquid-crystal mediated nanoparticle interactions and gel formation. *J. Chem. Phys.* **138**, 194903 (2013).

54. Foffano, G., Lintuvuori, J. S., Tiribocchi, A. & Marenduzzo, D. The dynamics of colloidal intrusions in liquid crystals: a simulation perspective. *Liq. Cryst. Rev.* **2**, 1–27 (2014).

55. Araki, T. & Tanaka, H. Colloidal aggregation in a nematic liquid crystal: Topological arrest of particles by a single-stroke disclination line. *Phys. Rev. Lett.* **97**, 1–4 (2006).